ARTICLE OPEN

Check for updates

On-chip spin-photon entanglement based on photon-scattering of a quantum dot

Ming Lai Chan [1]✉, Alexey Tiranov[1,3], Martin Hayhurst Appel [1,4], Ying Wang[1], Leonardo Midolo [1], Sven Scholz[2], Andreas D. Wieck [2], Arne Ludwig [2], Anders Søndberg Sørensen [1] and Peter Lodahl[1]

The realization of on-chip quantum interfaces between flying photons and solid-state spins is a key building block for quantum-information processors, enabling, e.g., distributed quantum computing, where remote quantum registers are interconnected by flying photons. Self-assembled quantum dots integrated into nanostructures are one of the most promising systems for such an endeavor thanks to their near-unity photon-emitter coupling and fast spontaneous emission rate. Here we demonstrate high-fidelity on-chip entanglement between an incoming photon and a stationary quantum-dot hole spin qubit. The entanglement is induced by sequential scattering of the time-bin encoded photon interleaved with active spin control within a microsecond, two orders of magnitude faster than those achieved in other solid-state platforms. Conditioning on the detection of a reflected photon renders the entanglement fidelity immune to the spectral wandering of the emitter. These results represent a major step towards realizing a quantum node capable of interchanging information with flying photons and on-chip quantum logic, as required for quantum networks and quantum repeaters.

INTRODUCTION

In a future quantum network[1], remote quantum nodes could be connected by a large web of entangled photons. Traditionally these photonic states have been generated probabilistically by fusing smaller states, which typically requires an exponential overhead of ancillary photons[2]. The advent of a deterministic quantum interface between light and matter promises to radically change this notion[3]. For such systems, a flying photon is funneled into a nanophotonic structure and interacts efficiently with a quantum emitter that hosts a single spin[4]. Coherent manipulation of the spin state entangles it with the photon, forming the basis for deterministic quantum gates and, e.g., the generation of photonic cluster states for quantum computing[5,6].

So far, significant progress has been made towards this goal, particularly the realization of spin-photon entanglement[7–14], spin-spin entanglement[13,15–18], single-photon switching and swap gate[19–21], and photon-photon entanglement[22–24] using various quantum emitters. Among these platforms, quantum dots (QDs) integrated into nanophotonic structures offer near-unity coupling to light ($\beta \geq 98\%$)[25] and a high photon-generation rate with near-unity purity and coherence[26,27]. Despite being proven to be an excellent single-photon source, an interface capable of producing entanglement between a flying photon and the QD has yet to be demonstrated. This approach to entanglement generation is particularly attractive in the context of long-distance quantum communication, as the pulse profile of an incoming photon is preserved upon scattering[28], which unlocks the prospects of interfacing distant emitters[17], realizing one-way quantum repeaters[29], and performing quantum gate operations between two photons[22] or QDs[30].

Here we step forward in this direction by demonstrating high-fidelity spin-photon entanglement between a guided photon and a QD spin embedded in a planar two-sided photonic-crystal waveguide (PCW). The entanglement is created in less than a microsecond by sequential scattering of time-bin encoded photons using a QD heavy-hole spin. Conditioning on the detection of a reflected photon renders the entanglement fidelity resistant to any residual spectral diffusion intrinsic to the emitter. The protocol can be extended to realize a fully deterministic entangling gate using single-sided waveguides[31].

RESULTS

Concept

The protocol used to induce entanglement between a flying photon and the localized QD spin is outlined in Fig. 1. A single photon pulse is prepared in a superposition of an early $|e\rangle$ and a late $|l\rangle$ time-bin $|\psi_p\rangle = \alpha|e\rangle + \beta|l\rangle$ for $\alpha, \beta \in \mathbb{C}$ constituting a flying qubit. The photon is launched into a waveguide where the embedded QD spin is initialized in $|\psi_s\rangle = |\Downarrow\rangle$. The protocol proceeds by alternating between coherent spin rotations $\hat{R}_y$ and single-photon scattering $\hat{S}$, cf. Fig. 1d. A $\hat{R}_y(\pi/2)$ pulse prepares the spin in a superposition of the two spin ground states $|\Downarrow\rangle$ and $|\Uparrow\rangle$, while $\hat{R}_y(\pi)$ serves two purposes: (1) to invert the spin in-between the two scattering events to create entanglement, and; (2) to prolong the spin coherence time by acting as a spin-echo pulse between the two equally long time-bins[32], when the spin is measured in the equatorial basis. $\hat{S}$ corresponds to the photon being reflected (transmitted) when the QD state is in $|\Uparrow\rangle$ ($|\Downarrow\rangle$) (Fig. 1c). When the flying photon is in an equatorial state, e.g., $\alpha = \beta = \frac{1}{\sqrt{2}}$, the ideal protocol results in the output state

$$|\psi_{\text{out}}\rangle \propto [\alpha|e \Downarrow\rangle - \beta|l \Uparrow\rangle]_{\mathbf{r}} + [\alpha|e \Uparrow\rangle - \beta|l \Downarrow\rangle]_{\mathbf{t}}$$
$$\equiv |\phi^-\rangle_{\mathbf{r}} + |\psi^-\rangle_{\mathbf{t}}, \tag{1}$$

which is a superposition of two spatially separated spin-photon Bell states. The subscript $\mathbf{r}$ ($\mathbf{t}$) indicates that the photon was

[1]Center for Hybrid Quantum Networks (Hy-Q), The Niels Bohr Institute, University of Copenhagen, DK-2100 Copenhagen Ø, Denmark. [2]Lehrstuhl für Angewandte Festörperphysik, Ruhr-Universität Bochum, Universitätsstraße 150, D-44801 Bochum, Germany. [3]Present address: Chimie ParisTech, Université PSL, CNRS, Institut de Recherche de Chimie Paris, 75005 Paris, France. [4]Present address: Cavendish Laboratory, University of Cambridge, JJ Thomson Avenue, Cambridge CB3 0HE, UK. ✉email: ming-lai.chan@nbi.ku.dk

a

b

c

d $\hat{R}_y(\frac{\pi}{2})$ $\hat{S}_e$ $\hat{R}_y(\pi)$ $\hat{S}_l$
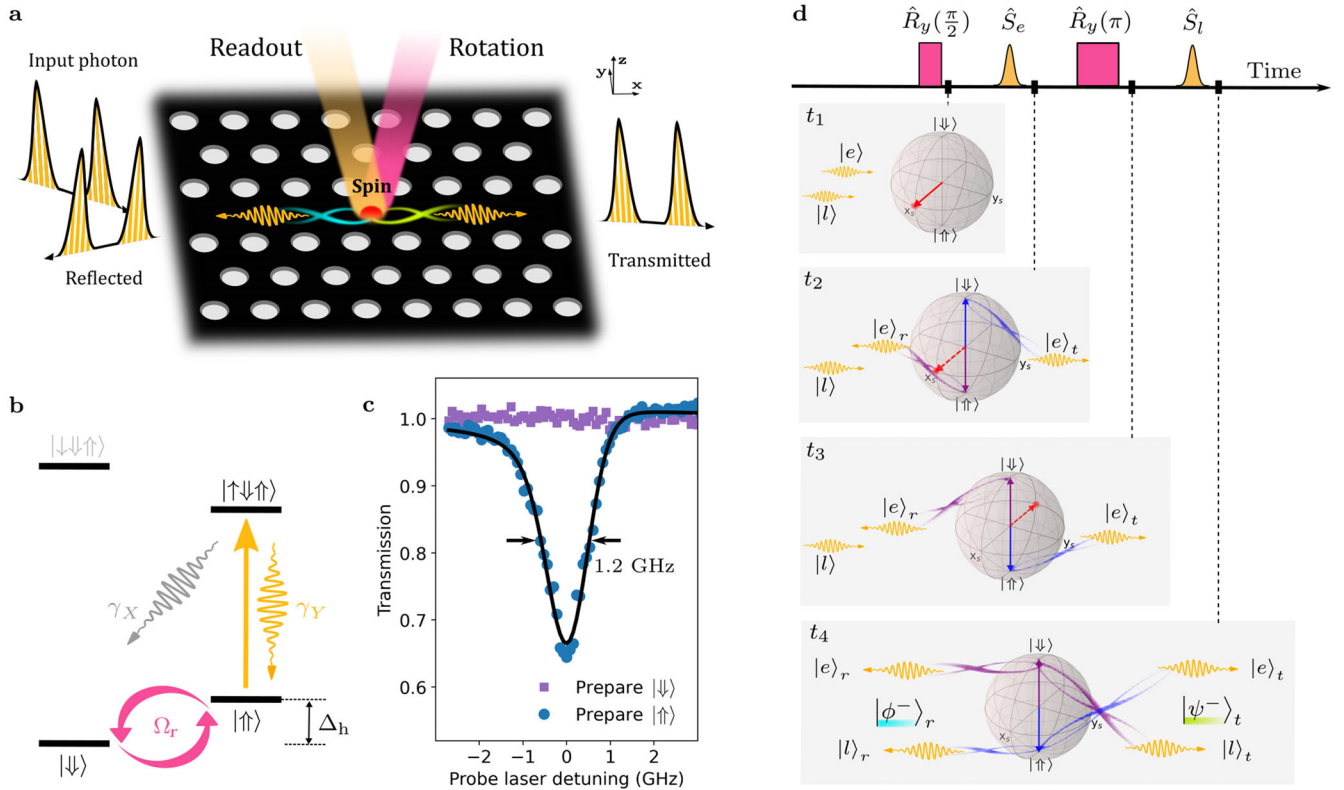
Fig. 1 Generation protocol of on-chip spin-photon entanglement. a A coherently controlled spin in a QD (red) inside a photonic-crystal waveguide, where a Bell state (cyan lines) is generated upon conditional detection of a reflected photon. **b** QD level diagram. The excited state $|\uparrow\Downarrow\Uparrow\rangle$ predominantly decays into $|\Uparrow\rangle$ with rate γ_Y as $\gamma_Y \gg \gamma_X$. The wavelength of the main transition is 945 nm. Coherent control of the metastable hole spin ground states (magenta arrows, Rabi frequency Ω_r) is realized via two-photon Raman processes by a detuned laser. **c** Single-photon transmission spectrum of the QD at $\mathbf{B}_y = 2$ T when preparing the spin state in either $|\Uparrow\rangle$ or $|\Downarrow\rangle$. **d** State evolution at different points in time during the protocol. At t_1, the QD spin (red) is prepared in a superposition state. At t_2, spin-dependent QD scattering occurs for the early time-bin $|e\rangle$. A π-rotation of the spin at t_3 is followed by a scattering of the late time-bin $|l\rangle$ photon pulse at t_4. The two distinct Bell states $|\phi^-\rangle$ ($|\psi^-\rangle$) are generated conditioned on the detection of a reflected (transmitted) photon.

reflected (transmitted) by the QD. By post-selecting the detection of a photon being reflected (transmitted), the Bell state in the first (second) bracket is prepared. We find that the conditional Bell-state fidelity can approach unity for our system due to the spectral selectivity of the QD that predominantly reflects photons resonant with the transition $|\Uparrow\rangle \rightarrow |\uparrow\Downarrow\Uparrow\rangle$, despite residual QD spectral diffusion visible from the broadened transmission dip in Fig. 1c (Supplementary Note 4).

Pre-calibration of the QD device
We subdivide the entanglement protocol into two separate experiments (Fig. 2). The first experiment probes the coherent nature of single-photon scattering (Fig. 2a), whereas the second experiment investigates the spin coherence with the built-in spin-echo sequence (Fig. 2c).

Probing single-photon interference
To demonstrate coherent scattering in the single-photon regime, we use a weak coherent state with a mean photon number per pulse $\bar{n} \ll 1$. We prepare a time-bin qubit using an asymmetric Mach–Zehnder interferometer where a photon is superposed between early and late temporal modes $|e\rangle$ and $|l\rangle$, and scatter off the QD spin initialized in $|\Uparrow\rangle$. If the input photon of spectral width $\sigma_o/2\pi$ is much narrower than the QD linewidth $\Gamma/2\pi$, the photon can be fully reflected due to destructive interference in transmission[33]. By interfering temporal modes of the reflected photon using the same interferometer and projecting on the X-basis $|\pm X\rangle_p = |e\rangle \pm |l\rangle$, the intensities $I_{\pm X}$ are measured, which are used

to estimate the photon visibility $V_p \equiv \frac{I_{+X}-I_{-X}}{I_{+X}+I_{-X}}$. Due to the finite interferometric delay $\tau_{\text{delay}} = 11.8$ ns, fluctuations occurring on longer timescales than τ_{delay} (i.e., spectral diffusion of QDs[34]) are essentially filtered out, as they influence the reflected phase of both time-bins equally. The single-photon interference is thus subject to only fast dephasing processes. Notably, in the single-photon regime ($\bar{n} \approx 0$), we found $V_p = \frac{\Gamma}{\Gamma+2\gamma_d}$ for the total decay rate $\Gamma \approx 2.48$ ns^{-1}[14] and γ_d is the pure dephasing rate (Supplementary Note 3). Here we measured a maximum value of $V_p = (89.7 \pm 0.4)\%$ which reduces linearly with $\bar{n}$ (Fig. 2b). Extrapolating a linear fit of V_p to the y-intercept where $\bar{n} = 0$ enables us to extract $\gamma_d \approx (0.099 \pm 0.004)$ ns^{-1}.

Spin-echo interferometry
The second experiment benchmarks the coherence of the internal hole spin qubit. Specifically, we perform a spin-echo sequence[35] consisting of two $\hat{R}_y(\pi/2)$ pulses separated by a $\hat{R}_y(\pi)$ pulse (Fig. 2c), which are implemented via the two-photon Raman scheme demonstrated in ref. [36] (see Methods). After the first $\hat{R}_y(\pi/2)$ pulse, due to fluctuating Overhauser nuclear fields[37] the spin state begins to fan out over the Bloch sphere equator (denoted by blue arrows) decaying with a spin dephasing time $T_2^* = 23.2$ ns[14]. Applying a $\hat{R}_y(\pi)$ pulse after time τ inverts the direction of spin precession, thus refocusing the spin state at $t = 2\tau$. The spin coherence is then probed by applying a second $\hat{R}_y(\pi/2)$ pulse, and scanning its phase ϕ_r followed by the spin readout, which projects the resulting spin state onto either the optically bright or dark state. The resulting interferometric fringe
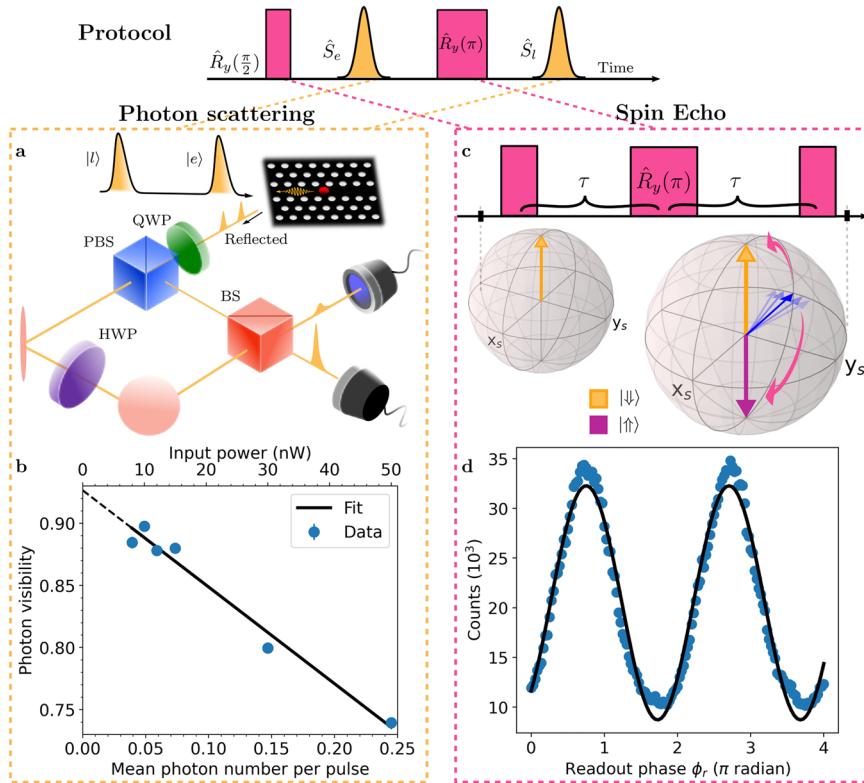
Fig. 2   Coherent single-photon scattering and spin control. a Setup for measuring photon visibility. The time-bin encoded qubit is reflected off the QD, which is initialized in the $|\Uparrow\rangle$ state. Upon entering the interferometer, the early time-bin is delayed, which interferes with the late time-bin, constituting a $|\pm X\rangle_p = |e\rangle \pm |l\rangle$ basis measurement. PBS, polarizing beam-splitter; BS, 50:50 beam-splitter; QWP (HWP), quarter (half) wave-plate. b Intensity visibility in photonic X-bases as a function of the mean photon number per pulse $\bar{n}$. The pure dephasing rate γ_d is extracted from the y-intercept where $\bar{n} = 0$. c The spin-echo sequence used to probe the spin coherence. The π-pulse is equally distant from the two π/2 pulses to eliminate inhomogeneous spin dephasing. The phase of the last π/2 pulse ϕ_r maps the equatorial state $|\Uparrow\rangle + e^{i\phi_r}|\Downarrow\rangle$ to the optically bright state $|\Uparrow\rangle$ ($\phi_r = \pi$) or dark state $|\Downarrow\rangle$ ($\phi_r = 0$). d Contrast between the spin $|\Downarrow\rangle$ and $|\Uparrow\rangle$ populations as a function of ϕ_r.

is depicted in Fig. 2d with an extracted visibility of $V_s = (57.5 \pm 0.4)\%$ at $\tau = 13$ ns, which is primarily limited by photo-induced incoherent spin processes[14]. V_s indicates how well the spin coherence is preserved and benchmarks the quality of spin-photon correlations on an equatorial basis.

Entanglement generation

Having characterized the coherences of both qubits, we are in a position to run the entanglement protocol. The spin is first prepared in a superposition state $|+X\rangle_s \propto |\Uparrow\rangle + |\Downarrow\rangle$ by a 3.5 ns $\hat{R}_y(\pi/2)$ pulse (Fig. 3a). The time-bin qubit is attenuated to $\bar{n} \approx 0.09$ before interacting with the QD (Supplementary Note 5). After sequential scattering of each time-bin, the reflected signal is collected and measured by the interferometer. Post-selecting the reflected photonic component carves out the output state [Eq. (1)] resulting in $|\phi^-\rangle_r$[38].

To determine the fidelity of the entangled state, we perform correlation measurements between the photonic modes and spin states. This involves projecting the entangled state on the $\hat{\sigma}_i^{(p)} \otimes \hat{\sigma}_i^{(s)}$ bases, where $i \in \{x, y, z\}$ denotes the Pauli operator, and the superscripts s (p) represent the spin and photonic qubits. The state of the reflected photon is detected in different time-bin windows after the interferometer, while the spin readout is performed by applying another rotation pulse $\hat{R}_i$ followed by optical driving of the main transition (see Methods; Fig. 3a).

For each experimental setting, we condition the detection of a reflected photon and the spin readout. The entanglement fidelity

is measured using[14]

$$\mathcal{F}_{Bell} = \frac{\langle\hat{P}_z\rangle}{2} + \frac{\langle\hat{M}_y\rangle - \langle\hat{M}_x\rangle}{4}, \quad (2)$$

where $\langle\hat{M}_i\rangle = \langle\hat{\sigma}_i^{(p)} \otimes \hat{\sigma}_i^{(s)}\rangle$ is the normalized contrast, and $\langle\hat{P}_z\rangle \equiv (1 + \langle\hat{M}_z\rangle)/2$. For measuring $\langle\hat{M}_{x/y}\rangle$, $\hat{R}_i = \hat{R}_{y/x}(\pi/2)$ is required for spin projection onto the equatorial state. Since the protocol now resembles a spin-echo sequence, the central $\hat{R}_y(\pi)$ pulse has an added benefit of spin-refocusing, whereas for Z-basis projections, spin echo is not necessary as $\langle\hat{P}_z\rangle$ is impervious to spin dephasing. As such, $|\langle\hat{M}_{x/y}\rangle|$ is dictated by the spin-echo visibility V_s, while $\langle\hat{P}_z\rangle$ largely reflects fidelity of the $\hat{R}_y(\pi)$ pulse F_π (Supplementary Note 2). Figure 3b–d show the raw (background corrected) coincidence counts in various readout bases. We record $\langle\hat{P}_z\rangle = (90.7 \pm 2.2)\%$, $\langle\hat{M}_x\rangle = (-58.8 \pm 4.5)\%$ and $\langle\hat{M}_y\rangle = (57.3 \pm 6.6)\%$, where residual background counts from laser rotation pulses were subtracted (Supplementary Note 9). The recorded values of $|\langle\hat{M}_{x/y}\rangle|$ and $\langle\hat{P}_z\rangle$ are consistent with measured V_s and F_π, respectively (see Methods). Using Eq. (2), we obtain a corrected Bell-state fidelity of $\mathcal{F}_{Bell} = (74.3 \pm 2.3)\%$ (raw fidelity of $(66 \pm 2)\%$), which far exceeds the classical limit of 50%, clearly demonstrating the presence of entanglement in the generated quantum state.

Theoretical modeling

To unravel the physical mechanisms limiting the experimental fidelity, we derive the fidelity (Supplementary Note 2) in the
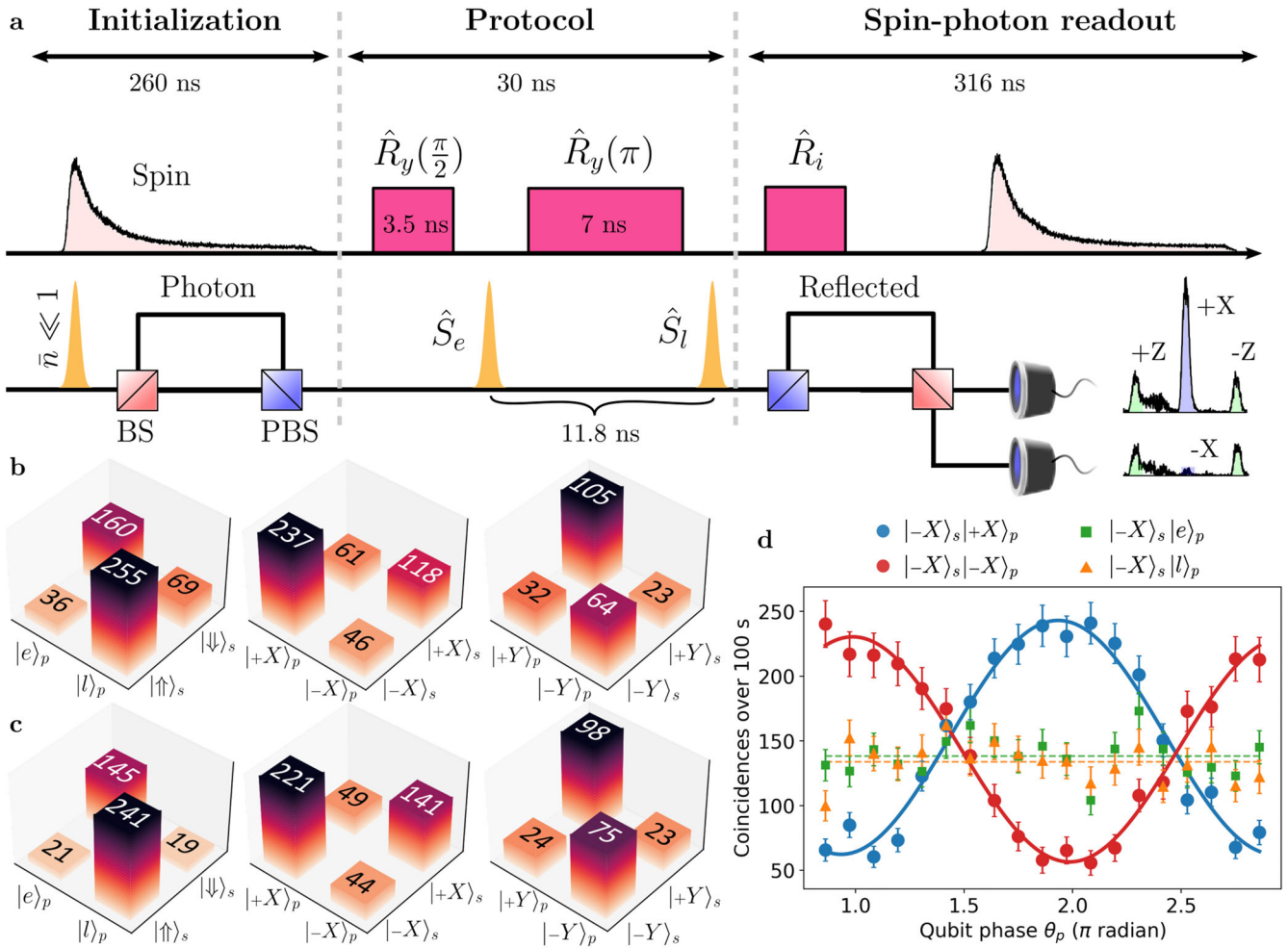
Fig. 3 Generation and verification of Bell states. a Experimental sequence consisting of the preparation of spin and photonic qubits, the entanglement protocol, and readout. The spin state is initialized and read out by optically driving the $|\Uparrow\rangle \leftrightarrow |\uparrow\Downarrow\Uparrow\rangle$ transition (pale red) and $\hat{R}_i$ controls the spin projection basis. The photonic qubit is prepared and measured by the same interferometer in either the Z-basis (green) or equatorial basis (blue) time window. **b** Raw two-photon coincidences measured during the photonic (p) readout window and spin (s) projections. **c** Measured two-photon coincidences corrected for laser background. **d** Visibility fringes of background-corrected two-photon coincidences as a function of the qubit phase θ_p when the spin state is projected on $|-X\rangle_s \propto |\Uparrow\rangle - |\Downarrow\rangle$. Circles (squares/triangles) correspond to projection on the photonic X-basis (±Z-basis). Solid curves are fits using $V_s \cos(\theta_p + \theta_{\text{offset}})$, and dashed lines are horizontal line fits.

perturbative limit of small errors,

$$\mathcal{F}^{\text{theory}}_{\text{Bell}} \approx 1 - \frac{\gamma_d}{\Gamma} - \frac{\Gamma^2}{4\Delta_h^2}, \tag{3}$$

where Δ_h is the ground-state splitting. Eq. (3) holds in the regime $\gamma_d \ll \Gamma \ll \Delta_h$ and assumes perfect manipulation of the hole spin state. In addition to being resilient to ground-state dephasing due to the built-in spin echo, the protocol is also impervious to errors arising from the spectral mismatch between the incoming optical pulse and the QD transition. This robustness is granted by the QD spectral reflectivity, which sifts out events where the photon interacts with the QD. The off-resonant frequency component of the incident pulse is transmitted without being detected, thus having no impact on the entanglement fidelity.

Using Eq. (3) with experimental parameters, the theoretical fidelity is estimated to be $\mathcal{F}^{\text{theory}}_{\text{Bell}} = 96.2\%$. Here the infidelity is attributed to decoherence from elastic phonon scattering[39]γ_d (3.7%) and reflection from the off-resonant spin state Γ/Δ_h (0.1%). The comparison to the experimental result indicates that several additional error mechanisms influence the experiment. The dominant cause is an incoherent photo-induced spin-flip

error leading to non-ideal spin rotations, as is visible on the spin-echo data (Fig. 2d). These rotation errors together amount to a total infidelity of 15% (Supplementary Note 2). Additional sources of error originate from driving-induced dephasing due to finite $\bar{n}$ (7.2%) and imperfect spin readout (2.7%), which are not intrinsic to the protocol. Taking these into account, we estimate a theoretical lower fidelity bound $\mathcal{F}^{\text{theory}}_{\text{total}} \geq 73.0\%$, which agrees with the experimental value within the error margins. Suppressing the photo-induced incoherent spin-flip processes is essential for improving the fidelity further. Encouragingly spin-rotation fidelities of 98.9% have been realized in the literature on electron spins[36] and could be combined with nuclear-spin cooling methods to realize T_2^* beyond 100 ns[40]. With these improvements, a near-unity entanglement fidelity is within reach.

DISCUSSIONS

The device performance is benchmarked by entanglement fidelity, protocol speed, and generation rate (Supplementary Note 7). In the present work, the demonstrated high entanglement fidelity (74%) is competitive with previous solid-state

Table 1. Key properties characterizing the QD hole spin and the waveguide device.

Parameter	Value
Emission wavelength	945 nm
External magnetic field $\mathbf{B}_y$	2 T
The total decay rate of the QD Γ	(2.48 ± 0.02) ns^{-1}[14]
Ground-state Zeeman splitting Δ_h	$2\pi \times 7.3$ GHz[14]
Optical cyclicity $C = \gamma_Y/\gamma_X$	14.7 ± 0.2[47]
Waveguide-coupling efficiency β	(0.865 ± 0.059)
Standard deviation in spectral diffusion fluctuation σ_e	$2\pi \times (332 \pm 15)$ MHz
Standard deviation in pulse spectral width σ_o	0.589 ns^{-1}
Pure dephasing rate γ_d	(0.099 ± 0.004) ns^{-1}
Spin-echo visibility V_s	(57.5 ± 0.4)%
Spin π-rotation fidelity F_π	(88.1 ± 3.8)%
Spin dephasing time T_2^*	(23.2 ± 1.4) ns[14]
Spin coherence time T_2^{echo}	(448 ± 37) ns[14]
Duration of the entanglement measurement sequence τ_{seq}	606 ns

Unreferenced parameters are documented in the Supplementary Material.

implementations[41,42], while the speed is improved. Indeed, the protocol operates on a sub-microsecond timescale (0.6 µs) which is at least two orders of magnitude faster than realized in SiV and atomic systems[13,43,44] as a consequence of the faster spin preparation time. The realized entanglement rate of 4.7 Hz of the present device can be readily improved by increasing the collection efficiency and reflectivity of the device (Supplementary Note 7).

Since the present implementation is conditioned on the detection of a reflected photon, the overall efficiency is bounded to at most 50%. By adopting a single-sided waveguide or equivalently coupling the incident light to both reflection and transmission ports via a stabilized interferometer, a fully deterministic spin-photon quantum gate[31] can eventually be realized. For a single-sided device, all photons are reflected but with a spin-dependent phase. As such, no post-selection is required though the fidelity will be sensitive to spectral drifts of the QD transition to the second order. This, however does not pose a fundamental limit to our platform, as near-lifetime-limited QD transitions in photonic structures compatible with the proposed scheme were recently reported[45].

We have demonstrated spin-photon entanglement by scattering an incoming photonic qubit off of a stationary QD spin. The system versatility is reflected by the fact that the same QD can also be operated as a source of multi-photon time-bin encoded entanglement generation[14]. Such versatile spin-photon interfaces constitute building blocks of one-way quantum repeaters[29]. Furthermore, a range of new integrated quantum photonics devices and functionalities could potentially be realized, e.g., a deterministic Bell-state analyzer or a photonic quantum non-demolition detector[31,46] that both rely on faithful coherent quantum state transfer from a flying photon to an emitter. The reflection-based scheme can be extended to realize non-local quantum entangling gates between distant quantum emitters[17]. Finally, applying the above protocol interleaved with spin rotations in a single-sided device would realize entanglement between two subsequently incoming photons, i.e., a deterministic photon–photon quantum gate[22], which is the most challenging quantum operation in photonics.

METHODS

Spin–photon interface

To achieve the highly efficient light-matter interaction required by the protocol, we prepare a QD embedded in a suspended PCW with two ports (Supplementary Note 1). The p–i–n heterostructure contains an intrinsic layer of self-assembled InAs QDs, enabling the electrical control of the QD charge state by applying a forward bias voltage. One experimental challenge is to simultaneously realize optical cycling transitions and spin control. This was recently achieved with a QD in a PCW under an in-plane magnetic field (Voigt geometry) by exploiting the inherent radiative asymmetry of the PCW[47]. We employ a positively charged exciton giving access to a meta-stable hole spin ground state that was characterized in the previous work[47]. An in-plane external magnetic field ($\mathbf{B}_y = 2$ T) Zeeman-splits the QD spin state into four energy levels, see Fig. 1b, where the linearly X- and Y-polarized dipoles form two Λ-systems. Thanks to the optical cyclicity of $C = \gamma_Y/\gamma_X \gg 1$ where the radiative decay rate γ_Y (γ_X) is strongly enhanced (suppressed) by the PCW, an effective two-level system $|\Uparrow\rangle \leftrightarrow |\uparrow\Downarrow\Uparrow\rangle$ resembling a "QD mirror" is realized. This leads to the spin-dependent reflection of photons into the same frequency and polarization modes, granting the spectral selectivity necessary for the entanglement protocol. The relevant system rates and parameters are summarized in Table 1.

Experimental setup

To perform high-fidelity entanglement experiments, the sample chip is cooled to 4.2 K inside a closed-cycle cryostat to suppress phonon scattering. A superconducting vector magnet provides a 2 T in-plane magnetic field enabling Raman transitions between two hole ground states. The sample is imaged with a 0.81 NA objective and brought to focus by translating 3 piezo positioners mounted beneath the sample. A DC voltage source provides a bias voltage at 1.148 V across the sample to populate QD charge states via tunnel coupling to a Fermi reservoir and control the charge environment.

The experiment utilizes the same laser setup as in ref. [14] with a few notable differences: two continuous waves (CW) lasers (linewidth < 10 kHz) are used for the creation of the photonic qubit, resonant excitation of the QD, and spin rotations. One of which is first directed to a double-pass acousto-optic modulator (AOM) setup followed by an electro-optical modulator (EOM; iXBlue NIR-MX800-LN-20) to generate 2 ns (FWHM) pulses for the photonic qubit. The non-diffracted light from the first AOM setup is then sent to a second AOM setup to create spin initialization and readout pulses (200 ns each) of the same laser frequency. The qubit laser pulses and QD emission are focused and collected at the same grating outcoupler using a cross-polarization scheme (Supplementary Note 1), while the readout laser is coupled directly on top of the QD (Fig. 1a).

A photonic qubit encoded in time-bins is created by passing the 2 ns pulses through an asymmetric Mach–Zehnder interferometer with a time delay of $\tau_{\text{delay}} = 11.82$ ns. Here we chose the FWHM duration for the input pulse to be 2 ns which exceeds the radiative lifetime of the optical transition $\Gamma^{-1} = 0.4$ ns for efficient single-photon scattering but is narrow enough to be fitted within the 11.8 ns time delay when combined with a 7 ns π-rotation pulse and 1 ns rise/fall time. The qubit phase θ_p can be scanned using a quarter-waveplate (QWP) and a linear polarizer. The reflected signal is then reinjected into the same interferometer and, subsequently two narrowband (3 GHz) etalon filters to remove the background from the rotation laser as well as QD phonon sidebands. The filtered signal then passes through a QWP and an EOM (not shown) which sets a 50/50 splitting ratio on the polarizing beam-splitter (see Fig. 2a). Since both the photonic qubit preparation and readout are performed via the same interferometer, the experiment becomes very robust against any

mechanical or thermal drift allowing near-unity interferometric visibility on a week-long timescale[14].

Another CW laser is used for coherent spin control. It is sent through a third AOM setup and another EOM, which is amplitude-modulated by a microwave source to create two sidebands with frequency difference matching the ground state splitting $\Delta_h/2\pi = 7.3$ GHz, thus effectively driving the ground-state spin manifold. The sidebands are red-detuned from the cycling transition by 350 GHz to avoid populating the excited states. The phase ϕ_r of the last microwave $\pi/2$-pulse is induced by a combination of a phase shifter and switches[14] with a phase offset of ~0.3π. The total pulse sequence duration is set to 606 ns.

Spin-photon state projections

As shown in Fig. 3a, the detection of an early (late) photon traversing through the short (long) path of the interferometer constitutes the $\hat{\sigma}_z^{(p)}$-basis measurement (green). The spin readout in the $\hat{\sigma}_z^{(s)}$-basis is performed by applying another rotation pulse $\hat{R}_i = \hat{R}_y(0)$ $(\hat{R}_y(\pi))$ followed by optical driving of the main transition. Similarly, projection on the $\hat{\sigma}_x^{(p)} \otimes \hat{\sigma}_x^{(s)}$ $(\hat{\sigma}_y^{(p)} \otimes \hat{\sigma}_y^{(s)})$ bases is performed by detecting photons in the middle time window (blue) at $\theta_p \approx 2\pi \equiv \theta_0$ $(\theta_p = \theta_0 + \pi/2)$ where the early and late time-bins between the short and long paths[14] interfere, followed by $\hat{R}_i = \hat{R}_y(\pm\pi/2)$ $(\hat{R}_x(\pm\pi/2))$ before the spin readout.

DATA AVAILABILITY

REFERENCES

1. Briegel, H. J., Browne, D. E., Dür, W., Raussendorf, R. & Van den Nest, M. Measurement-based quantum computation. *Nat. Phys.* **5**, 19–26 (2009).
2. Browne, D. E. & Rudolph, T. Resource-efficient linear optical quantum computation. *Phys. Rev. Lett.* **95**, 010501 (2005).
3. Uppu, R., Midolo, L., Zhou, X., Carolan, J. & Lodahl, P. Quantum-dot-based deterministic photon–emitter interfaces for scalable photonic quantum technology. *Nat. Nanotechnol.* **16**, 1308–1317 (2021).
4. Lodahl, P., Ludwig, A. & Warburton, R. J. A deterministic source of single photons. *Phys. Today* **75**, 44–50 (2022).
5. Lindner, N. H. & Rudolph, T. Proposal for pulsed on-demand sources of photonic cluster state strings. *Phys. Rev. Lett.* **103**, 113602 (2009).
6. Pichler, H., Choi, S., Zoller, P. & Lukin, M. D. Universal photonic quantum computation via time-delayed feedback. *Proc. Natl Acad. Sci. USA* **114**, 11362–11367 (2017).
7. Togan, E. et al. Quantum entanglement between an optical photon and a solid-state spin qubit. *Nature* **466**, 730–734 (2010).
8. Gao, W. B., Fallahi, P., Togan, E., Miguel-Sanchez, J. & Imamoğlu, A. Observation of entanglement between a quantum dot spin and a single photon. *Nature* **491**, 426–430 (2012).
9. De Greve, K. et al. Complete tomography of a high-fidelity solid-state entangled spin–photon qubit pair. *Nat. Commun.* **4**, 2228 (2013).
10. Schaibley, J. R. et al. Demonstration of quantum entanglement between a single electron spin confined to an inas quantum dot and a photon. *Phys. Rev. Lett.* **110**, 167401 (2013).
11. Schwartz, I. et al. Deterministic generation of a cluster state of entangled photons. *Science* **354**, 434–437 (2016).
12. He, Y. et al. Quantum state transfer from a single photon to a distant quantum-dot electron spin. *Phys. Rev. Lett.* **119**, 060501 (2017).
13. Nguyen, C. T. et al. Quantum network nodes based on diamond qubits with an efficient nanophotonic interface. *Phys. Rev. Lett.* **123**, 183602 (2019).
14. Appel, M. H. et al. Entangling a hole spin with a time-bin photon: a waveguide approach for quantum dot sources of multiphoton entanglement. *Phys. Rev. Lett.* **128**, 233602 (2022).
15. Delteil, A. et al. Generation of heralded entanglement between distant hole spins. *Nat. Phys.* **12**, 218–223 (2016).
16. Stockill, R. et al. Phase-tuned entangled state generation between distant spin qubits. *Phys. Rev. Lett.* **119**, 010503 (2017).
17. Daiss, S. et al. A quantum-logic gate between distant quantum-network modules. *Science* **371**, 614–617 (2021).
18. Dordevic, T. et al. Entanglement transport and a nanophotonic interface for atoms in optical tweezers. *Science* **373**, 1511–1514 (2021).
19. Sun, S., Kim, H., Luo, Z., Solomon, G. S. & Waks, E. A single-photon switch and transistor enabled by a solid-state quantum memory. *Science* **361**, 57–60 (2018).
20. Javadi, A. et al. Spin–photon interface and spin-controlled photon switching in a nanobeam waveguide. *Nat. Nanotechnol.* **13**, 398–403 (2018).
21. Bechler, O. et al. A passive photon–atom qubit swap operation. *Nat. Phys.* **14**, 996–1000 (2018).
22. Hacker, B., Welte, S., Rempe, G. & Ritter, S. A photon–photon quantum gate based on a single atom in an optical resonator. *Nature* **536**, 193–196 (2016).
23. Istrati, D. et al. Sequential generation of linear cluster states from a single photon emitter. *Nat. Commun.* **11**, 5501 (2020).
24. Thomas, P., Ruscio, L., Morin, O. & Rempe, G. Efficient generation of entangled multiphoton graph states from a single atom. *Nature* **608**, 677–681 (2022).
25. Arcari, M. et al. Near-unity coupling efficiency of a quantum emitter to a photonic crystal waveguide. *Phys. Rev. Lett.* **113**, 093603 (2014).
26. Tomm, N. et al. A bright and fast source of coherent single photons. *Nat. Nanotechnol.* **16**, 399–403 (2021).
27. Uppu, R. et al. Scalable integrated single-photon source. *Sci. Adv.* **6**, eabc8268 (2020).
28. Duan, L.-M. & Kimble, H. J. Scalable photonic quantum computation through cavity-assisted interactions. *Phys. Rev. Lett.* **92**, 127902 (2004).
29. Borregaard, J. et al. One-way quantum repeater based on near-deterministic photon-emitter interfaces. *Phys. Rev. X* **10**, 021071 (2020).
30. Mahmoodian, S., Lodahl, P. & Sørensen, A. S. Quantum networks with chiral-light–matter interaction in waveguides. *Phys. Rev. Lett.* **117**, 240501 (2016).
31. Borregaard, J., Sørensen, A. S. & Lodahl, P. Quantum networks with deterministic spin–photon interfaces. *Adv. Quantum Technol.* **2**, 1800091 (2019).
32. Tiurev, K. et al. High-fidelity multiphoton-entangled cluster state with solid-state quantum emitters in photonic nanostructures. *Phys. Rev. A* **105**, L030601 (2022).
33. Shen, J. T. & Fan, S. Coherent photon transport from spontaneous emission in one-dimensional waveguides. *Opt. Lett.* **30**, 2001–2003 (2005).
34. Kuhlmann, A. V. et al. Charge noise and spin noise in a semiconductor quantum device. *Nat. Phys.* **9**, 570–575 (2013).
35. Hahn, E. L. Spin echoes. *Phys. Rev.* **80**, 580–594 (1950).
36. Bodey, J. H. et al. Optical spin locking of a solid-state qubit. *npj Quantum Inf.* **5**, 95 (2019).
37. Urbaszek, B. et al. Nuclear spin physics in quantum dots: an optical investigation. *Rev. Mod. Phys.* **85**, 79–133 (2013).
38. Welte, S., Hacker, B., Daiss, S., Ritter, S. & Rempe, G. Cavity carving of atomic bell states. *Phys. Rev. Lett.* **118**, 210503 (2017).
39. Tighineanu, P., Dreeßen, C. L., Flindt, C., Lodahl, P. & Sørensen, A. S. Phonon decoherence of quantum dots in photonic structures: Broadening of the zero-phonon line and the role of dimensionality. *Phys. Rev. Lett.* **120**, 257401 (2018).
40. Jackson, D. M. et al. Optimal purification of a spin ensemble by quantum-algorithmic feedback. *Phys. Rev. X* **12**, 031014 (2022).
41. Tchebotareva, A. et al. Entanglement between a diamond spin qubit and a photonic time-bin qubit at telecom wavelength. *Phys. Rev. Lett.* **123**, 063601 (2019).
42. Kim, H., Bose, R., Shen, T. C., Solomon, G. S. & Waks, E. A quantum logic gate between a solid-state quantum bit and a photon. *Nat. Photonics* **7**, 373–377 (2013).
43. Bhaskar, M. K. et al. Experimental demonstration of memory-enhanced quantum communication. *Nature* **580**, 60–64 (2020).
44. Kalb, N., Reiserer, A., Ritter, S. & Rempe, G. Heralded storage of a photonic quantum bit in a single atom. *Phys. Rev. Lett.* **114**, 220501 (2015).
45. Pedersen, F. T. et al. Near transform-limited quantum dot linewidths in a broadband photonic crystal waveguide. *ACS Photonics* **7**, 2343–2349 (2020).
46. Witthaut, D., Lukin, M. D. & Sørensen, A. S. Photon sorters and QND detectors using single photon emitters. *Europhys. Lett.* **97**, 50007 (2012).
47. Appel, M. H. et al. Coherent spin-photon interface with waveguide induced cycling transitions. *Phys. Rev. Lett.* **126**, 013602 (2021).

ACKNOWLEDGEMENTS

AUTHOR CONTRIBUTIONS

M.L.C. and A.T. contributed equally to this work. M.L.C and A.T. performed the experiment, and theoretical analysis with help from A.S.S. Y.W. fabricated the device. A.L. and S.S. performed the heterostructure wafer growth with input from A.D.W. M.L.C. and A.T. analyzed the data with help from M.H.A. M.L.C., A.T., and P.L. wrote the paper with input from all authors. P.L., A.S.S., L.M., A.L., and A.D.W. supervised the project.

COMPETING INTERESTS

P.L. is the founder of the company Sparrow Quantum which commercializes single-photon sources. The remaining authors declare no competing interests.

ADDITIONAL INFORMATION

Supplementary information The online version contains supplementary material available at https://doi.org/10.1038/s41534-023-00717-5.

Correspondence and requests for materials should be addressed to Ming Lai Chan.

Reprints and permission information is available at http://www.nature.com/reprints

Publisher's note Springer Nature remains neutral with regard to jurisdictional claims in published maps and institutional affiliations.